

## Fourier analysis of near-field patterns generated by propagating polaritons

Minsoo Jang<sup>1,‡</sup>, Sergey G. Menabde<sup>1,\*‡</sup>, Fatemeh Kiani,<sup>2</sup> Jacob T. Heiden<sup>1</sup>,  
Vladimir A. Zenin<sup>3</sup>, N. Asger Mortensen<sup>4,5</sup>, Giulia Tagliabue,<sup>2</sup> and Min Seok Jang<sup>1,†</sup>

<sup>1</sup>*School of Electrical Engineering, Korea Advanced Institute of Science and Technology (KAIST), Daejeon 34141, Korea*

<sup>2</sup>*Laboratory of Nanoscience for Energy Technologies (LNET), School of Engineering (STI), EPFL, Lausanne 1015, Switzerland*

<sup>3</sup>*Center for Nano Optics, University of Southern Denmark, Odense DK-5230, Denmark*

<sup>4</sup>*POLIMA – Center for Polariton-driven Light-Matter Interactions, University of Southern Denmark, Odense DK-5230, Denmark*

<sup>5</sup>*Danish Institute for Advanced Study, University of Southern Denmark, Odense DK-5230, Denmark*

(Received 3 March 2024; revised 24 May 2024; accepted 3 July 2024; published 30 July 2024)

Scattering-type scanning near-field optical microscope (s-SNOM) has become an essential tool to study polaritons—quasiparticles of light coupled to collective charge oscillations—via direct probing of their near field with a spatial resolution far beyond the diffraction limit. However, extraction of the polariton’s complex propagation constant from the near-field images requires subtle considerations that have not received the necessary attention so far. In this study, we discuss important yet overlooked aspects of the near-field analysis. First, we experimentally demonstrate that the sample orientation inside the s-SNOM may significantly affect the near-field interference pattern of mid-infrared polaritons, leading to an error in momentum measurement up to 7.7%, even for the modes with an effective index of 12.5. Second, we establish a methodology to correctly extract the polariton damping rate from the interference fringes depending on their origin—i.e., the s-SNOM nanotip or the material edge. Overall, our work provides a unified framework for the accurate extraction of the polariton momentum and damping from the near-field interference fringes.

DOI: 10.1103/PhysRevApplied.22.014076

### I. INTRODUCTION

Material characterization is crucial for advancing technologies in a wide range of fields; this also holds true for optics. In particular, polaritons, the quasiparticles born out of coupling between light and excitations in material (collective oscillations of free carriers, phonons, excitons, etc.), provide comprehensive information about the electrodynamic response of the employed material [1–9]. At the same time, low-dimensional surface polaritons promise diverse nanophotonic applications due to the strong field confinement, delivering enhanced light-matter interaction [9–16]. The surface polaritons possess tremendous application potential such as high-density data storage [17], surface-enhanced Raman spectroscopy [18,19], thermal emission control [20–22], negative refraction [23], biosensing [24,25], and beam steering [26–28].

Scattering-type scanning near-field optical microscope (s-SNOM) offers a breakthrough method for direct measurement of the polaritonic near-field amplitude and

phase with a spatial resolution of inherently nonradiating excitations beyond the diffraction limit—a regime that cannot be probed by far-field instrumentation [29]. In a conventional s-SNOM experiment, both excitation and detection of surface polaritons are typically carried out via light scattering by the sharp nanotip of the atomic force microscope (AFM), resulting in a near-field interference pattern that carries information about the complex propagation constant [1,3,30–37]. In this study, we rigorously analyze the extraction of the complex propagation constant from the near-field data and demonstrate that commonly accepted approximations for the polariton momentum analysis may lead to significant quantitative errors.

While the conventional approach of direct fitting of the near-field signal can yield good qualitative results [33,36,38], we show that the Fourier analysis of the near-field interference in momentum space is a rigorous and convenient method readily applicable even for mixed signals formed by a superposition of several propagating modes. Importantly, we demonstrate that the polaritonic damping rate can be estimated from the near-field interference fringes as well. However, this is not given by the width of their Fourier spectrum as implicitly assumed in

\*Contact author: menabde@kaist.ac.kr

†Contact author: jang.minseok@kaist.ac.kr

‡These authors contributed equally to this work

previous works [33,39,40]. We also highlight the different analysis methods for the polaritons launched by the s-SNOM nanotip and the material edge, which are required for the correct extraction of damping in each case. Furthermore, we elaborate on the usually dismissed effects of the azimuthal and incidence angles between the s-SNOM excitation beam and the sample when polaritons are launched by the material edge, and show that these effects should be considered for rigorous analysis of the near-field interference.

The importance of the sample orientation relative to the excitation beam has been explored in earlier work for polaritons with relatively low effective indices [8,41–44], i.e., when  $k_p(\omega) \sim k_0 = \omega/c$ , where  $k_p$  is the polariton momentum and  $k_0$  is the momentum in free space. However, sample orientation has typically been neglected for near-field probing of the highly confined mid-infrared (mid-IR) polaritons, such as hyperbolic phonon-polaritons (HPP) in thin hexagonal boron nitride (hBN) [45] or alpha-phase molybdenum trioxide ( $\alpha\text{-MoO}_3$ ) [2,37], including our own prior works on hBN [39] and on  $\alpha\text{-MoO}_3$  [40] and many other works studying mid-IR polaritons.

For the experiments, we use hBN on evaporated and monocrystalline gold where HPP is excited by light scattering at the atomically clear edges of hBN or gold crystals [46], in addition to the tip-excited HPP. For the edge-launched polaritons, we demonstrate the discrepancy of the measured polariton momentum up to 7.7% compared with the actual value, even when the HPP effective index  $n_{\text{eff}}(\omega) = k_p(\omega)/k_0(\omega)$  is as large as 12.5. This deviation is caused by the oblique incidence of the excitation beam, so that its phase at the edge (where polaritons are launched) is different from its phase at the nanotip (which creates a reference background). The phase delay depends on the distance from the edge and the angle between the excitation beam and the propagation direction of the edge-launched polaritons. At the same time, we demonstrate that the analysis of the tip-launched polaritons provides the correct momentum, but is impeded by significant damping due to the diverging wavefront. Thus, our results constitute a framework for accurate analysis of polariton momentum and damping based on near-field images and are particularly important for a growing number of studies where the near-field data is used to measure properties of novel polaritonic materials [2,4,5,37,47,48].

## II. NEAR-FIELD COMPONENTS OF POLARITON INTERFERENCE

The operation principle of s-SNOM is based on the interferometric detection of the near-field signal from a sample surface, which is coupled to the far field via scattering by a sharp AFM nanotip while scanning the sample in a tapping mode [29]. The commonly used reflection mode

of the s-SNOM setup exploits the same beam path for both illumination and collection of the scattering; therefore, the excitation beam is constantly focused on the nanotip, as illustrated in Fig. 1(a). However, in the mid-IR s-SNOM setup, the polaritonic material edge is also illuminated unless it is located considerably distant from the tip. This is because the diffraction-limited illumination spot size is on the order of the free-space wavelength [49],  $\lambda_0$ , while the polariton wavelength,  $\lambda_p$ , can be 10–100 times less than  $\lambda_0$  due to the high effective index of the polariton mode. Therefore, the required scan size (and, thus, the maximum distance between the edge and the tip) rarely exceeds the boundaries of the illumination beam. Thus, the beam scatters at both the metallic nanotip and the material edge, resulting in a local electric field at the nanotip,  $\mathbf{E}_{\text{tip}}$ , given as a superposition of the incident field,  $\mathbf{E}_i$ , and the polariton fields,  $\mathbf{E}_{\text{pt}}$  and  $\mathbf{E}_{\text{pe}}$ , from the tip-launched and the edge-launched modes, respectively, so that

$$\mathbf{E}_{\text{tip}} = \mathbf{E}_i + \mathbf{E}_{\text{pt}} + \mathbf{E}_{\text{pe}}. \quad (1)$$

The resulting near-field interference pattern, thus, carries the information about the polariton mode but generally consists of several components of different nature, which must be disentangled to properly extract the complex propagation constant of the polariton.

The contribution of the tip-launched polariton is nonzero only when the excited polariton is returned to the tip, for example, by reflecting from the material edge. By considering only a single straight material edge at a distance  $x$  from the tip [Fig. 1(b)], the contribution of the tip-launched polariton can be expressed as follows:

$$\mathbf{E}_{\text{pt}}(x) = \tilde{c}_{\text{pt}} \tilde{r} \sqrt{\frac{\lambda_p}{2(x+x_0)}} e^{i\tilde{k}_p 2x} \mathbf{E}_i, \quad (2)$$

where  $\tilde{c}_{\text{pt}}$  is the complex excitation efficiency of the tip-launched polariton,  $\tilde{r}$  is the complex polariton reflection coefficient at the edge, and  $\tilde{k}_p = k_p + ik'_p$  is the complex polariton wave-vector,  $k_p = 2\pi/\lambda_p$ . Since the tip-launched polariton has a radially diverging wavefront, an additional geometrical correction term  $\sqrt{\lambda_p/(x+x_0)}$  is included to account for the power conservation in the effectively 2D polaritonic wave. Recognizing that the initial mode size at the moment of excitation is  $\sim\lambda_p$ , we estimate that  $x_0 \sim \lambda_p/2$ . We note that this correction term effectively resolves the ambiguity of the  $x$ -axis origin for the fringe analysis and allows for avoiding amplitude divergence at  $x = 0$  of a simple geometric correction parameter  $1/\sqrt{x}$ , as used in previous works [8,31,33,37,44].

At the same time, the edge-excited polariton exhibits different propagation dynamics in terms of the field damping and the wavefront shape. Considering the distance between the tip and the material edge,  $x$ , the incident field at the material edge is  $\mathbf{E}_0 = \mathbf{E}_i \exp(-ik_0 x \cos \varphi \cos \alpha)$ , where  $\alpha$  is the angle of incidence to the material surface,

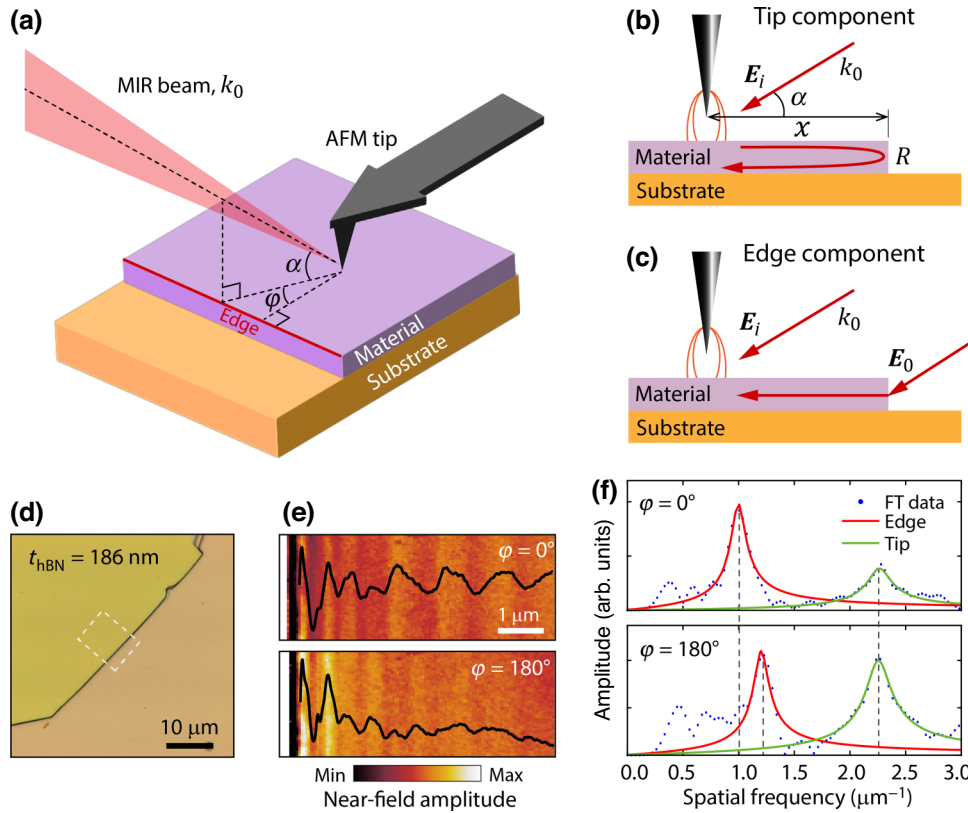


FIG. 1. Schematics of s-SNOM and the analyzing method. (a) Illustration of the experimental setup where p-polarized MIR beam with wave-vector  $k_0$  is focused on the AFM tip at the angle  $\alpha = 30^\circ$  with respect to material surface. The edge rotation angle  $\varphi$  is defined as the angle between the plane of incidence and the normal to the edge. Side view of the experimental setup showing the two excitation mechanisms: (b) by the AFM tip and (c) by the edge. (d) Optical microscope image of a 186-nm-thick hBN on an evaporated gold substrate. (e) Near-field amplitude map at an excitation wave number of  $1500 \text{ cm}^{-1}$  and angle  $\varphi = 0^\circ$  and  $180^\circ$ . The black curve shows the averaged data in the direction perpendicular to the fringes. The s-SNOM images were obtained within the area marked by the white dashed rectangle in (d). (f) Fourier spectra (blue dots) of the near-field amplitude in (e) integrated across the fringes. A Lorentzian-like line-shape is used to fit the spectra of the edge component (red) and the tip component (green). The black dashed line indicates the Lorentzian peak position.

and  $\varphi$  is the azimuthal angle of incidence compared with the straight edge [Figs. 1(a)–1(c)]. The phase delay  $k_0 x \cos \varphi \cos \alpha$  is observed as a frequency shift in the momentum space [50]. At the tip position, the field from the edge-launched polariton is given by [51]

$$\mathbf{E}_{\text{pe}}(x) = \tilde{c}_{\text{pe}} e^{i k_p x} \mathbf{E}_0 = \tilde{c}_{\text{pe}} e^{i(\tilde{k}_p - \Delta k)x} \mathbf{E}_i, \quad (3)$$

where  $\tilde{c}_{\text{pe}}$  is the complex excitation efficiency of the edge-launched polariton, and  $\Delta k = k_0 \cos \varphi \cos \alpha$  indicates the different phases of the excitation wavefront at the edge and tip positions that cause a shift of the spatial frequency of the interference pattern imaged by the s-SNOM. It should be noted that the reverse light pass, i.e., when the incident

beam excites polaritons at the tip, which are then scattered by the edge to the far field, is described with a similar equation. Therefore, this contribution is incorporated into the arbitrary parameter  $\tilde{c}_{\text{pe}}$ .

The scattered field from the tip,  $\mathbf{E}$ , which is measured by the s-SNOM, is proportional to the local electric field  $\mathbf{E}_{\text{tip}}$  under the tip [Eq. (1)] and its effective polarizability  $\tilde{\alpha}_{\text{eff}}$  describes the near-field coupling between the tip and the sample surface [49]. From Eqs. (1)–(3), by recognizing that the tip-coupling and the edge-coupling of the polaritons are both highly inefficient processes (i.e.,  $|\tilde{c}_{\text{pt}}|, |\tilde{c}_{\text{pe}}| \ll 1$ ) [31] and taking the Taylor series expansion of  $|\mathbf{E}|$  up to the first order terms in  $\tilde{c}_{\text{pe}}$  and  $\tilde{c}_{\text{pt}}$ ,  $|\mathbf{E}|$  can be approximated as follows:

$$|\mathbf{E}| \approx |\tilde{\alpha}_{\text{eff}}| \left[ 1 + |\tilde{c}_{\text{pe}}| e^{-k' p x} \cos[(k_p - \Delta k)x + \psi_{\text{pe}}] + |\tilde{c}_{\text{pt}}| |\tilde{r}| \sqrt{\frac{\lambda_p}{2(x + x_0)}} e^{-2k' p x} \cos(2k_p + \psi_{\text{pt}}) \right] |\mathbf{E}_i|, \quad (4)$$

where  $\psi_{\text{pe}} = \arg(\tilde{c}_{\text{pe}})$ ,  $\psi_{\text{pt}} = \arg(\tilde{c}_{\text{pt}}\tilde{r})$ , and  $x_0 = \lambda_p/2$ . The first term in Eq. (4) is the direct contribution of the incident beam, and the second and third oscillatory terms arise from the incident light interfering with the tip-launched polaritons and the edge-launched polaritons, respectively. We note that the p-polarized illumination beam provides the most efficient excitation of the vertically elongated nanotip, which scatters mostly the out-of-plane component of the electric field. Therefore, in the following discussion, we consider only the out-of-plane electric field of phonon-polaritons in hBN, which are TM-polarized modes [52].

### III. POLARITON MOMENTUM ANALYSIS

Fourier transformation (FT) provides a convenient method to analyze surface polariton properties from the measured near-field images. Most notably, it enables discrimination between the edge-launched and the tip-launched polariton contributions since they produce interference patterns with largely different momenta,  $k_p - \Delta k$  and  $2k_p$ , respectively, as expected from Eq. (4). By separately analyzing the Fourier spectrum of each excitation component, it is possible to reliably and quantitatively determine the complex wave-vector.

Based on Eq. (4), the  $|E|$  profile from the edge-launched component has the form of a damped harmonic oscillator,  $f(x) = Ae^{-2\pi\gamma x} \cos(2\pi\nu x)$ , with the analytically derived Fourier spectrum,  $F(s)$ , given by a Lorentzian-like function, i.e.,

$$F(s) = A \left( \frac{\gamma + is}{(\gamma + is)^2 + \nu^2} \right). \quad (5)$$

Consequently, fitting the Fourier spectrum of the near-field interference pattern with Eq. (5) enables the extraction of not only the spatial frequency  $\nu_p = k_p/2\pi$  but also the damping rate of the polariton  $\gamma_p = k'_p/2\pi$ . In the following analysis, we use Eq. (5) to fit the Fourier spectra of the near-field pattern from both components. Although  $f(x)$  is only an approximation for the signal from the edge-launched component, Eq. (5) still perfectly fits the Fourier spectrum, accurately providing a value of  $\nu_p$ .

To demonstrate the near-field signal from the differently launched polaritons, we performed s-SNOM measurements near the edge of a 186-nm-thick hBN crystal on an evaporated gold substrate [Fig. 1(d)]. When hBN is placed on gold, the HPP couples with its mirror image in the metal, producing an approximately twice as confined hyperbolic image phonon-polariton (HIP), which becomes the fundamental mode [53,54].

Figure 1(e) shows the near-field amplitude maps in the vicinity of the hBN edge at  $\alpha = 30^\circ$  for  $\varphi = 0^\circ$  and  $180^\circ$ , where tip- and edge-launched polaritons produce a complex interference pattern. The analyzed interference profiles (black curves) are obtained by averaging the near-field maps in the direction parallel to the fringes. Baseline

fitting by a low-order (less than or equal to third-order) polynomial is employed to eliminate minor but inevitable background fluctuations, and then the Fourier spectrum of the near-field profile is calculated starting from the second maximum. When the background fluctuations are severe, up to the fifth-order polynomial may be employed. However, even in this case, the background spatial frequency is much smaller than that of the polaritonic interferences; thereby, the extracted data is not affected. The first interference maximum (closest to the edge) is mostly due to the strong near-field scattering at the sharp material edge and, thus, must be excluded from this analysis. Additionally, after background extraction, by appending the real-space data with zeros beyond the measurement area where polariton fringes converge to zero, it is possible to increase the resolution in momentum space even with small scan sizes. Moreover, frequency filtering enables the separation of background and noise, facilitating polariton analysis even in low-quality near-field images.

In agreement with expectations based on Eq. (1), the Fourier spectrum of the near-field amplitude [gray lines in Fig. 1(f) and fitted Lorentzian-like line-shapes] exhibits two clear peaks: the higher frequency peak centered at  $2\nu_p = 2.26(\pm 0.01) \mu\text{m}^{-1}$  is due to the tip-launched polaritons and does not depend on  $\varphi$ , while the lower frequency peak due to the edge-launched polaritons is centered at  $\nu_p \mp \Delta\nu = 0.99(\pm 0.02)$  and  $1.24(\pm 0.01) \mu\text{m}^{-1}$  for  $\varphi = 0^\circ$  and  $180^\circ$ , respectively, showing a strong dependency on  $\varphi$ . Here and henceforth, the values inside the parentheses provide the 95% confidence interval for the experimental data fitting. The spatial frequency difference between the two angles is  $0.25 \mu\text{m}^{-1}$ , which is very close to the expected value of  $2\Delta\nu = 2\nu_0 \cos \alpha \cos \varphi = 0.26 \mu\text{m}^{-1}$ , where  $\nu_0 = k_0/2\pi = \lambda_0^{-1}$ . Consequently, the spatial frequency of the HIP can be estimated from the edge-launched contribution when the angle-dependent frequency shift is accounted for, providing  $\nu_p = 1.12 \mu\text{m}^{-1}$ , which closely agrees with  $\nu_p = 1.13 \mu\text{m}^{-1}$  extracted from the tip-launched component.

The full width at half maximum (FWHM) of the fitted spectra of the edge-launched HIP [red Lorentzian-like line-shapes in Fig. 1(f)] is almost the same for both  $\varphi = 0^\circ$  and  $180^\circ$ :  $\text{FWHM} = 0.22(\pm 0.02)$  and  $0.24(\pm 0.03) \mu\text{m}^{-1}$ , respectively. The tip-launched HIP spectra [green Lorentzian-like profiles in Fig. 1(f)] are expected to be more than two times wider compared with those of the edge-launched HIP because of doubled damping  $\gamma_p$  and the additional geometrical damping factor. Surprisingly, their FWHM are less than expected:  $0.35(\pm 0.02)$  and  $0.36(\pm 0.01) \mu\text{m}^{-1}$  for  $\varphi = 0^\circ$  and  $180^\circ$ , respectively. We believe that this might be due to the dependence of  $\tilde{c}_{\text{pt}}$ ,  $\tilde{\alpha}_{\text{eff}}$ , and  $\tilde{r}$  on the tip-edge distance  $x$ , which is expected near the edge [52], where the fast-decaying tip-launched polaritons are most

pronounced. Therefore, only the edge-launched HIP spectra can be used to accurately calculate the polariton damping, as will be discussed in detail later in the text.

To experimentally estimate the range of the momentum extraction error as a function of angle  $\varphi$ , we use a very thin ( $\approx 20$  nm) monocrystalline gold flake covered with hBN, as shown in Figs. 2(a) and 2(b). We perform s-SNOM scans across the atomically clear edge of the gold crystal, which excites polariton modes with much higher efficiency than the AFM tip or the hBN edge, owing to its much larger scattering cross-section [31]. Furthermore, the tip-launched polaritons experience little reflection by the underlying gold edge (i.e.,  $|\tilde{r}| \ll 1$ ) and, thus, practically do not contribute to the interference pattern [39,40]. Consequently, the near-field patterns arise mainly due to the interference between the edge-launched polaritons and the incident light, further simplifying the analysis.

Figure 2(c) displays the near-field maps over the 76-nm-thick hBN flake at the excitation frequency of  $1530\text{ cm}^{-1}$  for various angles  $\varphi$ . The Fourier spectra of the HPP fringes on the right-hand side of the gold crystal edge [Fig. 2(c)] are shown in Fig. 2(d), clearly demonstrating the spatial frequency shift: the peak position of the fitted Lorentzian-like curve (red) is  $1.75(\pm 0.02)$ ,  $1.87(\pm 0.01)$ ,  $1.96(\pm 0.02)$ , and  $2.06(\pm 0.02)\text{ }\mu\text{m}^{-1}$  at  $\varphi=0^\circ$ ,  $45^\circ$ ,  $135^\circ$  and  $180^\circ$ , respectively. The maximum spatial frequency difference between  $0^\circ$  and  $180^\circ$  is

$0.29\text{ }\mu\text{m}^{-1}$ , which is very close to the analytically estimated value  $2\nu_0 \cos \alpha \cos \varphi = 0.26\text{ }\mu\text{m}^{-1}$  determined from Eq. (4).

The extracted HPP spatial frequencies for all measured cases are summarized in Fig. 2(e), clearly demonstrating the blueshift when  $\varphi$  increases. The corresponding deviation of the measured spatial frequency is analyzed in Fig. 2(f). The black solid line shows the analytically predicted shift  $\nu_0 \cos \alpha \cos \varphi$ , while the measured momentum is shown by the average value at different excitation frequencies (normalized by  $\nu_0$ ). The relative error for the extracted polariton momentum can, thus, be calculated as an inverse of the effective mode index:  $\cos \alpha \cos \varphi / n_{\text{eff}}$ .

Experimental results show the deviation of the extracted polariton momentum from the actual value by as much as 7.7%, even for the HPP with a relatively large effective index of 12.5. Therefore, even when  $n_{\text{eff}} > 10$ , the previously ignored orientation-mediated deviation of the near-field interference must be considered. We also note that the interference fringes due to the HIP appear on the left-hand side of the gold edge [Fig. 2(c)], where the hBN flake is atop the Au crystal. In this region, the surface plasmon on gold (also launched by the gold edge) results in a noticeable fluctuation in the near-field amplitude. The presence of surface plasmons could potentially jeopardize the precise extraction of polariton momentum by interfering with the HPP, making it necessary to exercise special caution in similar experiments.

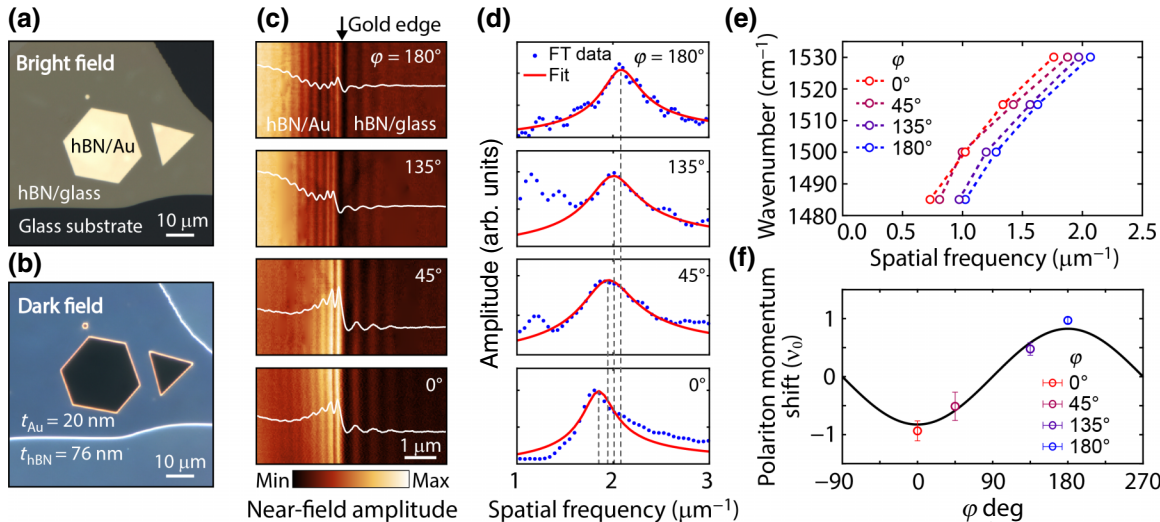


FIG. 2. Relationship between the orientation angle and the spatial frequency shift. (a) Bright-field and (b) dark-field optical microscope images of a 76-nm-thick hBN flake transferred on top of a monocrystalline gold flake. (c) Near-field amplitude map near the gold crystal edge at different orientation angles  $\varphi$ . The polariton modes to the left-hand side of the edge are the hBN/gold HIP, and the ones to the right-hand side are the hBN/glass HPP. (d) Fourier spectra of HPP shown in (c) (blue dots), fitted by a Lorentzian-like curve (red line). The spectral peak position of HPP is shifting as the angle changes (gray dashed line). (e) Measured dispersion of HPP at different edge orientations (data points), showing the significant frequency shift for HPP. (f) HPP momentum shift normalized by  $\nu_0$ , depending on the edge orientation angle  $\varphi$ , obtained from the data shown in (e). The data points show the average momentum at a given  $\varphi$ , and the error bar displays the standard deviation. The black solid line is the theoretically predicted deviation,  $\nu_0 \cos \varphi \cos \alpha$ .

#### IV. POLARITON DAMPING ANALYSIS

We proceed with the methodology for the extraction of the polariton damping from the near-field interference fringes. As discussed earlier, fitting the Fourier spectrum of the near-field interference pattern using Eq. (5) allows for an extraction of not only the spatial frequency  $\nu_p$  but also the damping rate of the polariton  $\gamma_p$ , albeit only for the edge-launched component. With the assumption of  $\gamma_p \ll \nu_p$ , which holds for polaritons in most van der Waals crystals [40], Eq. (5) provides the maximal Fourier amplitude  $|F(\nu_p)| \approx A/2\gamma_p$ . By denoting the FWHM as  $\Gamma$  and keeping only the lowest-order nonzero terms, we arrive at the identity

$$\frac{A}{4\gamma_p} \approx \frac{|F(\nu_p)|}{2} = \left| F\left(\nu_p \pm \frac{\Gamma}{2}\right) \right| \approx \frac{A}{2\gamma_p} \sqrt{\frac{1}{1 + (\Gamma/2\gamma_p)^2}}. \quad (6)$$

To satisfy the above equation, the relationship between FWHM and the damping rate  $\gamma_p$  should be

$$\gamma_p = \text{Im} \{ \tilde{k}_p \} / 2\pi \approx \frac{\sqrt{3}}{6} \Gamma. \quad (7)$$

It is worth emphasizing that the derived relationship between  $\gamma_p$  and  $\Gamma$  is largely different from the assumption of  $\gamma_p = \Gamma$  that only holds for truly Lorentzian spectra in a form  $F_L(s) = 0.5\Gamma/[s^2 + (0.5\Gamma)^2]$ .

The relationship described by Eq. (7) can be verified by a full-wave numerical simulation, as illustrated in Fig. 3(a). The interference between the TM-polarized incident field,  $E_i$ , and the polaritons it excites at the gold edge produces the fringes of  $|E_z|$  [red curves in Figs. 3(b) and 3(c)], as predicted by Eq. (4). The background signal fluctuations at the HPP side [blue dashed curve in Fig. 3(b)] are caused by the self-interference of incident light upon reflection and is filtered out in the s-SNOM experiments [Fig. 2(c)].

Figures 3(d) and 3(e) show the Fourier spectra of  $|E_z|$  with removed background fluctuations (blue dots),

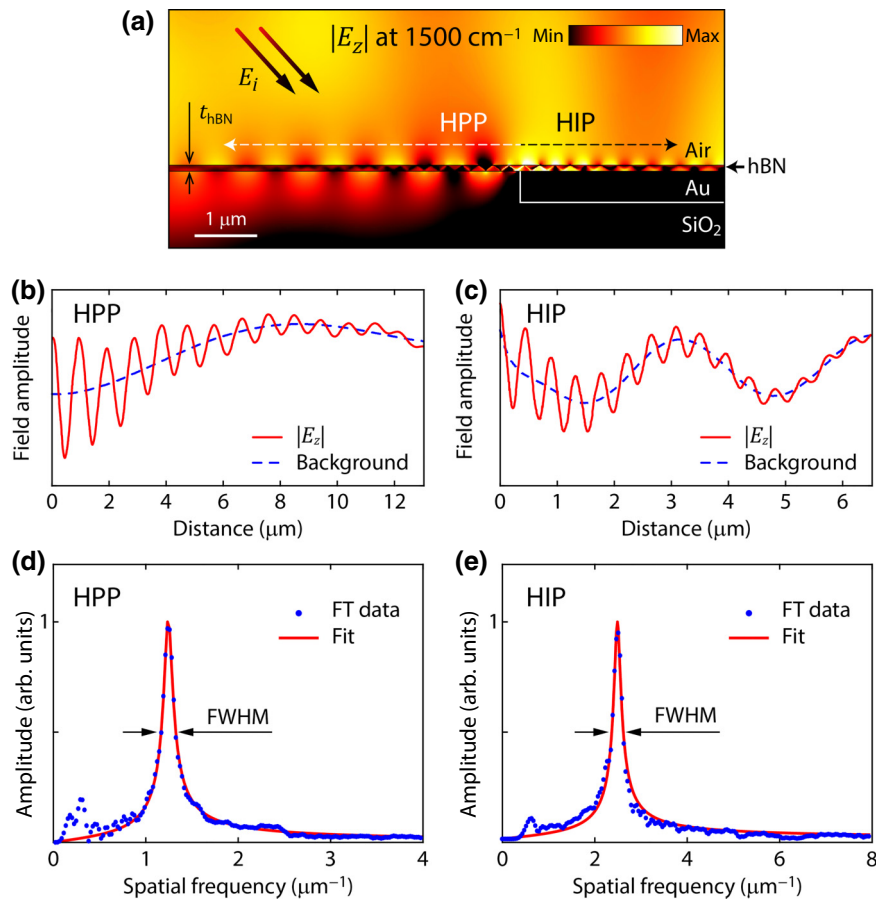


FIG. 3. Comparison of the FWHM and the fitting parameters via the simulation results. (a) Numerically calculated field interference of the HPP and HIP, excited at the gold edge with  $1500 \text{ cm}^{-1}$ ;  $t_{\text{hBN}} = 80 \text{ nm}$ . The incident plane wave illuminates the shown area at the incident angle  $\alpha = 30^\circ$ . The  $|E_z|$  profile (red solid curves) of the (b) HPP and (c) HIP extracted at 70 nm above the hBN surface [dashed line in (a)]. The blue dashed line shows the background of the interference field. The Fourier spectra of  $|E_z|$  (blue dots) of the (d) HPP and (e) HIP fitted by the Lorentzian-like line-shape given by Eq. (5) (red curves).

perfectly fitted by the curve given by Eq. (5) (red solid). Fitted damping rate  $\gamma_p = 0.045$  and  $0.071 \mu\text{m}^{-1}$  for HPP and HIP, respectively, while the FWHM of the Fourier spectra  $\Gamma = 0.16(\pm 0.01)$  and  $0.24(\pm 0.02) \mu\text{m}^{-1}$ , or  $\approx 2\sqrt{3}$  times larger compared with the damping rate as predicted by Eq. (7). The same tendency is observed for the HIP analyzed in Fig. 1: the FWHM values for  $\varphi = 0^\circ$  and  $180^\circ$  are  $0.22(\pm 0.02)$  and  $0.24(\pm 0.03) \mu\text{m}^{-1}$ , respectively, while  $\gamma_p = 0.062$  and  $0.067 \mu\text{m}^{-1}$ , revealing the same  $2\sqrt{3}$  difference.

At the same time, the Fourier analysis of the interference pattern from the tip-launched polaritons requires more elaborate consideration since it is not rigorously described by the simple expression given by Eq. (5) due to the geometric term. The diverging wavefront of the tip-launched polaritons effectively leads to a faster decay of the field amplitude, resulting in a broader linewidth in the Fourier domain, which can be seen in Fig. 1(f).

Figure 4(a) illustrates the Fourier spectrum of the near-field fringes above the hBN flake on evaporated gold (inset). To filter out a parasitic near-field signal from the strong scattering at the hBN edge, the interference pattern is analyzed starting from the second maximum (indicated by the white arrow in the inset). The two peaks in the spectrum correspond to the edge and tip components, while the tip component is much stronger due to the weaker excitation of the edge component at the given angle  $\varphi = 180^\circ$ . Fitting the spectrum of the tip component using Eq. (5), with the double travel path  $2x$ , yields  $\gamma_p = \gamma/2 = 0.114(\pm 0.01)$  and  $v_p = v/2 = 2.40(\pm 0.01) \mu\text{m}^{-1}$ , while the analytical values for HIP mode are  $\gamma_{p,\text{HIP}} = 0.059$  and  $v_{p,\text{HIP}} = 2.38 \mu\text{m}^{-1}$ , indicating the presence of extra damping due to the diverging wavefront.

In order to disentangle the polariton damping from the geometrical decay factor, we analyze the near-field signal in real space. The interference pattern generated purely by the tip-launched polariton [gray line in Fig. 4(b)] is restored from the spectrum in Fig. 4(a) by taking the inverse Fourier transform of the spectrally filtered data [shaded area in Fig. 4(a)]. Then, the near-field pattern can be directly fitted by the two functions without [Eq. (8)] and with [Eq. (9)] the geometrical decay factor, i.e.,

$$f(x) = e^{-4\pi\gamma_p x} \cos\left(\frac{4\pi x}{\lambda_p}\right), \quad (8)$$

$$f(x) = \frac{e^{-4\pi\gamma_p x} \cos(4\pi x/\lambda_p)}{\sqrt{2(x+x_0)}}, \quad (9)$$

where  $x_0$  is assumed to be 0 and  $\lambda_p/2$ . Both Eqs. (8) and (9) well fit the inversed FT data, correctly providing the value of  $\lambda_p = 0.42 \mu\text{m}$ . However, the fitted damping rates are drastically different. Equation (8) yields  $\gamma_p = 0.114(\pm 0.001) \mu\text{m}^{-1}$ , very similar to

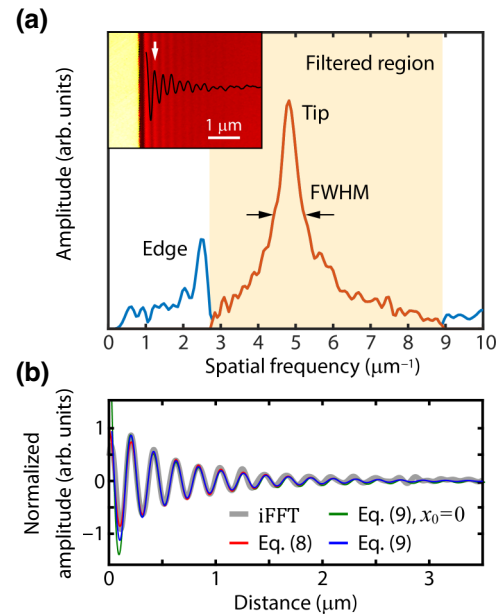


FIG. 4. Damping analysis for the tip component. (a) Fourier spectrum of the near-field amplitude profile from 89-nm-thick hBN on evaporated gold at  $1510 \text{ cm}^{-1}$  (inset). The signal is truncated at the second maximum (white arrow) and the spectrum is filtered (orange-shaded region) to isolate the near-field signal from the tip component. (b) Inverse Fourier transform data of the extracted tip component (gray line) and the fittings from the results with a geometric term when  $x_0 = 0$  and  $\lambda_p/2$  (green and blue line, respectively) and without the geometric damping term (red line).

the fitted parameter of Eq. (5) in momentum space. Equation (9) with the geometric term when  $x_0 = \lambda_p/2$  provides  $\gamma_p = 0.088(\pm 0.001) \mu\text{m}^{-1}$ , which is in better agreement with the analytically predicted HIP damping  $\gamma_{p,\text{HIP}} = 0.059(\pm 0.001) \mu\text{m}^{-1}$ . At the same time, Eq. (9) with  $x_0 = 0$  yields  $\gamma_p = 0.126(\pm 0.003) \mu\text{m}^{-1}$ , which is larger than the two previous cases because of the divergence at zero. Thus, although all the considered cases seemingly provide a very good fit to the real-space data [Fig. 4(b)], only Eq. (9) with the initial mode size correction provides a simple yet most accurate model for analyzing the near-field interference pattern generated by the tip-launched polariton. We emphasize that the spectral filtering of the tip component in the Fourier space is required, followed by the inverse FFT and the fitting of the real-space data.

## V. CONCLUSION

In summary, we demonstrate a rigorous analysis of the near-field interference patterns obtained in s-SNOM experiments with propagating polaritons, highlighting the important considerations for accurate measurement of the polariton propagation constant. First, we show that the

near-field interference pattern can be analyzed in Fourier space, allowing for the independent analysis of several modes typically present in the near-field experiment and accurate extraction of the damping coefficient if the mode is launched by the material edge. Second, we show that the sample orientation may affect the near-field interference pattern and introduce a significant error in the extracted polariton momentum. We experimentally show that this error can be as large as 7.7%, even for modes with an effective index exceeding 10. Our results demonstrate the importance of the sample direction in s-SNOM and the necessity to consider the sample orientation in near-field analysis of the polaritons. Next, we analytically investigate the correlation between the FWHM of the Fourier spectrum and the damping of the propagating polariton, revealing their correlation with a specific ratio  $2\sqrt{3}$ . Finally, we elucidated the contribution of the geometric term to the damping of the tip component in both real space and Fourier space, emphasizing the crucial importance of the geometric term for fringes analysis.

## ACKNOWLEDGMENTS

This research was supported by the National Research Foundation of Korea (NRF) grants funded by the Ministry of Science and ICT (Grant No. NRF-2022R1A2C2092095) and the Ministry of Education (Grant No. NRF-2021R1I1A1A01057510). This work was also supported under the framework of an international cooperation program managed by the NRF (Grant No. 2022K2A9A2A23 000272, FY2022). The Center for Polariton-Driven Light-Matter Interactions (POLIMA) is funded by the Danish National Research Foundation (Project No. DNRF165). F.K. and G.T. acknowledge the support of the Swiss National Science Foundation (Eccezzenza Grant No. 194181). This work was also supported by the BK21 FOUR Program through the NRF funded by the Ministry of Education.

## APPENDIX A: SAMPLE PREPARATION AND CHARACTERIZATION

Evaporated gold substrates were made by a thermal evaporation method with an evaporation velocity of 0.2 Å/s and the sample stage rotating at 1 Hz to reduce surface roughness. The Au crystals were grown on borosilicate glass via a gap-assisted and halide-assisted synthesis [46], which enables the growth of ultrathin flakes compared with the previous halide-free method [55]. Two glass substrates were cleaned with acetone and then ethanol within an ultrasonic bath for 10 min. These were subsequently immersed into the growth solution with a small tilt angle and a gap between them of approximately 43 μm. 50 μl of KBr and 50 μl of KCl solutions (0.5 mM) were added to the growth solution. The solution was stirred and then rested for 1 min before immersing the capped

tube containing the solution into a light-tight water bath at 90 °C for 8 to 25 h. After removing the substrates from the solution, they were rinsed thoroughly with ethanol and deionized water to remove loosely attached microflakes and any remaining reagents. Finally, nitrogen was used to blow the samples dry. The hBN bulk material was purchased from a commercial source (2D semiconductors, USA), and hBN layers were mechanically exfoliated from the bulk single crystal and then transferred by the polydimethylsiloxane (PDMS) stamp onto the substrates. Near-field measurements were performed with a commercial s-SNOM (Neaspec GmbH) coupled with a tunable quantum cascade laser (Daylight Solutions, MIRcat). The Pt/Ir coated metallic AFM tips (NanoWorld, ARROW-NCPT) were used in a tapping mode with a frequency  $\Omega$  around 270 kHz and an amplitude of 70 nm. The interferometric signal was demodulated at a third harmonic frequency of  $3\Omega$  to remove background signal fluctuations. The thickness of the hBN flakes was simultaneously measured by the AFM.

- [1] S. Dai, Z. Fei, Q. Ma, A. Rodin, M. Wagner, A. McLeod, M. Liu, W. Gannett, W. Regan, and K. Watanabe, Tunable phonon polaritons in atomically thin van der Waals crystals of boron nitride, *Science* **343**, 1125 (2014).
- [2] Z. Zheng, N. Xu, S. L. Oscurato, M. Tamagnone, F. Sun, Y. Jiang, Y. Ke, J. Chen, W. Huang, and W. L. Wilson, A mid-infrared biaxial hyperbolic van der Waals crystal, *Sci. Adv.* **5**, eaav8690 (2019).
- [3] G. Álvarez-Pérez, T. G. Folland, I. Errea, J. Taboada-Gutiérrez, J. Duan, J. Martín-Sánchez, A. I. Tresguerres-Mata, J. R. Matson, A. Bylinkin, and M. He, Infrared permittivity of the biaxial van der Waals semiconductor  $\alpha$ -MoO<sub>3</sub> from near-and far-field correlative studies, *Adv. Mater.* **32**, 1908176 (2020).
- [4] J. Taboada-Gutiérrez, G. Álvarez-Pérez, J. Duan, W. Ma, K. Crowley, I. Prieto, A. Bylinkin, M. Autore, H. Volkova, and K. Kimura, Broad spectral tuning of ultra-low-loss polaritons in a van der Waals crystal by intercalation, *Nat. Mater.* **19**, 964 (2020).
- [5] S. Chen, P. Leng, A. Konečná, E. Modin, M. Gutierrez-Amigo, E. Vicentini, B. Martín-García, M. Barra-Burillo, I. Niehues, and C. Maciel Escudero, Real-space observation of ultraconfined in-plane anisotropic acoustic terahertz plasmon polaritons, *Nat. Mater.* **22**, 860 (2023).
- [6] J. Chen, M. Badioli, P. Alonso-González, S. Thongrattanasiri, F. Huth, J. Osmond, M. Spasenović, A. Centeno, A. Pesquera, and P. Godignon, Optical nanooptical imaging of gate-tunable graphene plasmons, *Nature* **487**, 77 (2012).
- [7] Z. Fei, A. Rodin, G. O. Andreev, W. Bao, A. McLeod, M. Wagner, L. Zhang, Z. Zhao, M. Thiemens, and G. Dominguez, Gate-tuning of graphene plasmons revealed by infrared nano-imaging, *Nature* **487**, 82 (2012).
- [8] F. Hu, Y. Luan, M. Scott, J. Yan, D. Mandrus, X. Xu, and Z. Fei, Imaging exciton-polariton transport in MoSe<sub>2</sub> waveguides, *Nat. Photonics* **11**, 356 (2017).

- [9] S. Kim, S. G. Menabde, V. W. Brar, and M. S. Jang, Functional mid-infrared polaritonics in van der Waals crystals, *Adv. Opt. Mater.* **8**, 1901194 (2020).
- [10] D. Basov, M. Fogler, and F. García de Abajo, Polaritons in van der Waals materials, *Science* **354**, aag1992 (2016).
- [11] J. Duan, N. Capote-Robayna, J. Taboada-Gutiérrez, G. Álvarez-Pérez, I. Prieto, J. Martín-Sánchez, A. Y. Nikitin, and P. Alonso-González, Twisted nano-optics: manipulating light at the nanoscale with twisted phonon polaritonic slabs, *Nano Lett.* **20**, 5323 (2020).
- [12] S. Kim, J. Y. Kim, M. S. Jang, and V. W. Brar, Electrical modulation of high-Q guided-mode resonances using graphene, *Carbon Trends* **8**, 100185 (2022).
- [13] S. Kim, S. G. Menabde, J. D. Cox, T. Low, and M. S. Jang, Ultracompact electro-optic waveguide modulator based on a graphene-covered  $\lambda/1000$  plasmonic nanogap, *Opt. Express* **29**, 13852 (2021).
- [14] P. Li, I. Dolado, F. J. Alfaro-Mozaz, F. Casanova, L. E. Hueso, S. Liu, J. H. Edgar, A. Y. Nikitin, S. Vélez, and R. Hillenbrand, Infrared hyperbolic metasurface based on nanostructured van der Waals materials, *Science* **359**, 892 (2018).
- [15] S. Kim, M. S. Jang, V. W. Brar, K. W. Mauser, L. Kim, and H. A. Atwater, Electronically tunable perfect absorption in graphene, *Nano Lett.* **18**, 971 (2018).
- [16] S. Han, S. Kim, S. Kim, T. Low, V. W. Brar, and M. S. Jang, Complete complex amplitude modulation with electronically tunable graphene plasmonic metamolecules, *ACS Nano* **14**, 1166 (2020).
- [17] J. Zhang, L. Zhang, and W. Xu, Surface plasmon polaritons: physics and applications, *J. Phys. D: Appl. Phys.* **45**, 113001 (2012).
- [18] B. Sharma, R. R. Frontiera, A.-I. Henry, E. Ringe, and R. P. Van Duyne, SERS: Materials, applications, and the future, *Mater. Today* **15**, 16 (2012).
- [19] H. J. Han, S. H. Cho, S. Han, J. S. Jang, G. R. Lee, E. N. Cho, S. J. Kim, I. D. Kim, M. S. Jang, and H. L. Tuller, Synergistic integration of chemo-resistive and SERS sensing for label-free multiplex gas detection, *Adv. Mater.* **33**, 2105199 (2021).
- [20] G. Lu, C. R. Gubbin, J. R. Nolen, T. Folland, M. J. Tadjer, S. De Liberato, and J. D. Caldwell, Engineering the spectral and spatial dispersion of thermal emission via polariton–phonon strong coupling, *Nano Lett.* **21**, 1831 (2021).
- [21] G. R. Jaffe, G. R. Holdman, M. S. Jang, D. Feng, M. A. Kats, and V. W. Brar, Effect of dust and hot spots on the thermal stability of laser sails, *Nano Lett.* **23**, 6852 (2023).
- [22] G. R. Holdman, G. R. Jaffe, D. Feng, M. S. Jang, M. A. Kats, and V. W. Brar, Thermal runaway of silicon-based laser sails, *Adv. Opt. Mater.* **10**, 2102835 (2022).
- [23] X. Su, T. Huang, B. Zheng, J. Wang, X. Wang, S. Yan, X. Wang, and Y. Shi, Atomic-scale confinement and negative refraction of plasmons by twisted bilayer graphene, *Nano Lett.* **22**, 8975 (2022).
- [24] L. Jiang, K. V. Kong, S. He, and K. T. Yong, Plasmonic biosensing with nano-engineered van der Waals interfaces, *ChemPlusChem* **87**, e202200221 (2022).
- [25] K. M. Song, S. Kim, S. Kang, T. W. Nam, G. Y. Kim, H. Lim, E. N. Cho, K. H. Kim, S. H. Kwon, and M. S. Jang, Microcellular sensing media with ternary transparency states for fast and intuitive identification of unknown liquids, *Sci. Adv.* **7**, eabg8013 (2021).
- [26] T. Xu, C. Wang, C. Du, and X. Luo, Plasmonic beam deflector, *Opt. Express* **16**, 4753 (2008).
- [27] J. Siegel, S. Kim, M. Fortman, C. Wan, M. A. Kats, P. W. Hon, L. Sweatlock, M. S. Jang, and V. W. Brar, Electrostatic steering of thermal emission with active metasurface control of delocalized modes, *Nat. Commun.* **15**, 3376 (2024).
- [28] J. Y. Kim, J. Park, G. R. Holdman, J. T. Heiden, S. Kim, V. W. Brar, and M. S. Jang, Full  $2\pi$  tunable phase modulation using avoided crossing of resonances, *Nat. Commun.* **13**, 2103 (2022).
- [29] X. Chen, D. Hu, R. Mescall, G. You, D. Basov, Q. Dai, and M. Liu, Modern scattering-type scanning near-field optical microscopy for advanced material research, *Adv. Mater.* **31**, 1804774 (2019).
- [30] S. Dai, Q. Ma, T. Andersen, A. Mcleod, Z. Fei, M. Liu, M. Wagner, K. Watanabe, T. Taniguchi, and M. Thiemens, Subdiffractive focusing and guiding of polaritonic rays in a natural hyperbolic material, *Nat. Commun.* **6**, 6963 (2015).
- [31] S. Dai, Q. Ma, Y. Yang, J. Rosenfeld, M. D. Goldflam, A. McLeod, Z. Sun, T. I. Andersen, Z. Fei, and M. Liu, Efficiency of launching highly confined polaritons by infrared light incident on a hyperbolic material, *Nano Lett.* **17**, 5285 (2017).
- [32] A. Ambrosio, M. Tamagnone, K. Chaudhary, L. A. Jaurregui, P. Kim, W. L. Wilson, and F. Capasso, Selective excitation and imaging of ultraslow phonon polaritons in thin hexagonal boron nitride crystals, *Light: Sci. Appl.* **7**, 27 (2018).
- [33] A. J. Giles, S. Dai, I. Vurgaftman, T. Hoffman, S. Liu, L. Lindsay, C. T. Ellis, N. Assefa, I. Chatzakis, and T. L. Reinecke, Ultralow-loss polaritons in isotopically pure boron nitride, *Nat. Mater.* **17**, 134 (2018).
- [34] G. Ni, d. A. McLeod, Z. Sun, L. Wang, L. Xiong, K. Post, S. Sunku, B.-Y. Jiang, J. Hone, and C. R. Dean, Fundamental limits to graphene plasmonics, *Nature* **557**, 530 (2018).
- [35] A. Nikitin, P. Alonso-González, S. Vélez, S. Mastel, A. Centeno, A. Pesquera, A. Zurutuza, F. Casanova, L. Hueso, and F. H. Koppens, Real-space mapping of tailored sheet and edge plasmons in graphene nanoresonators, *Nat. Photonics* **10**, 239 (2016).
- [36] A. Bylinkin, M. Schnell, M. Autore, F. Calavalle, P. Li, J. Taboada-Gutiérrez, S. Liu, J. H. Edgar, F. Casanova, and L. E. Hueso, Real-space observation of vibrational strong coupling between propagating phonon polaritons and organic molecules, *Nat. Photonics* **15**, 197 (2021).
- [37] W. Ma, P. Alonso-González, S. Li, A. Y. Nikitin, J. Yuan, J. Martín-Sánchez, J. Taboada-Gutiérrez, I. Amenabar, P. Li, and S. Vélez, In-plane anisotropic and ultra-low-loss polaritons in a natural van der Waals crystal, *Nature* **562**, 557 (2018).
- [38] X. Ni, G. Carini, W. Ma, E. M. Renzi, E. Galiffi, S. Wasserroth, M. Wolf, P. Li, A. Paarmann, and A. Alù, Observation of directional leaky polaritons at anisotropic crystal interfaces, *Nat. Commun.* **14**, 2845 (2023).

- [39] S. G. Menabde, S. Boroviks, J. Ahn, J. T. Heiden, K. Watanabe, T. Taniguchi, T. Low, D. K. Hwang, N. A. Mortensen, and M. S. Jang, Near-field probing of image phonon-polaritons in hexagonal boron nitride on gold crystals, *Sci. Adv.* **8**, eabn0627 (2022).
- [40] S. G. Menabde, J. Jahng, S. Boroviks, J. Ahn, J. T. Heiden, D. K. Hwang, E. S. Lee, N. A. Mortensen, and M. S. Jang, Low-loss anisotropic image polaritons in van der Waals crystal  $\alpha$ -MoO<sub>3</sub>, *Adv. Opt. Mater.* **10**, 2201492 (2022).
- [41] K. P. Wong, X. Hu, T. W. Lo, X. Guo, K. H. Fung, Y. Zhu, and S. P. Lau, Edge-orientation dependent nanoimaging of mid-infrared waveguide modes in high-index PtSe<sub>2</sub>, *Adv. Opt. Mater.* **9**, 2100294 (2021).
- [42] K. J. Kaltenecker, E. Krauss, L. Casses, M. Geisler, B. Hecht, N. A. Mortensen, P. U. Jepsen, and N. Stenger, Mono-crystalline gold platelets: a high-quality platform for surface plasmon polaritons, *Nanophotonics* **9**, 509 (2020).
- [43] A. Mancini, L. Nan, F. J. Wendisch, R. Berté, H. Ren, E. Cortés, and S. A. Maier, Near-field retrieval of the surface phonon polariton dispersion in free-standing silicon carbide thin films, *ACS Photonics* **9**, 3696 (2022).
- [44] L. N. Casses, K. J. Kaltenecker, S. Xiao, M. Wubs, and N. Stenger, Quantitative near-field characterization of surface plasmon polaritons on monocrystalline gold platelets, *Opt. Express* **30**, 11181 (2022).
- [45] J. D. Caldwell, I. Aharonovich, G. Cassabois, J. H. Edgar, B. Gil, and D. Basov, Photonics with hexagonal boron nitride, *Nat. Rev. Mater.* **4**, 552 (2019).
- [46] F. Kiani and G. Tagliabue, High aspect ratio Au microflakes via gap-assisted synthesis, *Chem. Mater.* **34**, 1278 (2022).
- [47] Z. Zheng, J. Chen, Y. Wang, X. Wang, X. Chen, P. Liu, J. Xu, W. Xie, H. Chen, and S. Deng, Highly confined and tunable hyperbolic phonon polaritons in van der Waals semiconducting transition metal oxides, *Adv. Mater.* **30**, 1705318 (2018).
- [48] N. C. Passler, X. Ni, G. Hu, J. R. Matson, G. Carini, M. Wolf, M. Schubert, A. Alù, J. D. Caldwell, and T. G. Folland, Hyperbolic shear polaritons in low-symmetry crystals, *Nature* **602**, 595 (2022).
- [49] G. Álvarez-Pérez, K. V. Voronin, V. S. Volkov, P. Alonso-González, and A. Y. Nikitin, Analytical approximations for the dispersion of electromagnetic modes in slabs of biaxial crystals, *Phys. Rev. B* **100**, 235408 (2019).
- [50] L. N. Casses, B. Zhou, Q. Lin, A. Tan, D.-P. B.-F. de Mongex, K. J. Kaltenecker, S. Xiao, M. Wubs, and N. Stenger, Full quantitative near-field characterization of strongly coupled exciton-plasmon polaritons in thin-layered WSe<sub>2</sub> on a monocrystalline gold platelet, arXiv preprint [arXiv:2403.18655](https://arxiv.org/abs/2403.18655) (2024).
- [51] A. Huber, N. Ocelic, D. Kazantsev, and R. Hillenbrand, Near-field imaging of mid-infrared surface phonon polariton propagation, *Appl. Phys. Lett.* **87**, 081103 (2005).
- [52] L. Mester, A. A. Govyadinov, and R. Hillenbrand, High-fidelity nano-FTIR spectroscopy by on-pixel normalization of signal harmonics, *Nanophotonics* **11**, 377 (2021).
- [53] I.-H. Lee, M. He, X. Zhang, Y. Luo, S. Liu, J. H. Edgar, K. Wang, P. Avouris, T. Low, and J. D. Caldwell, Image polaritons in boron nitride for extreme polariton confinement with low losses, *Nat. Commun.* **11**, 3649 (2020).
- [54] S. G. Menabde, J. T. Heiden, J. D. Cox, N. A. Mortensen, and M. S. Jang, Image polaritons in van der Waals crystals, *Nanophotonics* **11**, 2433 (2022).
- [55] E. Krauss, R. Kullock, X. Wu, P. Geisler, N. Lundt, M. Kamp, and B. Hecht, Controlled growth of high-aspect-ratio single-crystalline gold platelets, *Cryst. Growth Des.* **18**, 1297 (2018).